MICROBIOLOGY

In situ monitoring of exopolymer-dependent Mn mineralization on bacterial surfaces

Thaïs Couasnon[1]*, Damien Alloyeau[2†], Bénédicte Ménez[1], François Guyot[3], Jean-Marc Ghigo[4], Alexandre Gélabert[1†]

Bacterial biomineralization is a widespread process that affects cycling of metals in the environment. Functionalized bacterial cell surfaces and exopolymers are thought to initiate mineral formation, however, direct evidences are hampered by technical challenges. Here, we present a breakthrough in the use of liquid-cell scanning transmission electron microscopy to observe mineral growth on bacteria and the exopolymers they secrete. Two *Escherichia coli* mutants producing distinct exopolymers are investigated. We use the incident electron beam to provoke and observe the precipitation of Mn-bearing minerals. Differences in the morphology and distribution of Mn precipitates on the two strains reflect differences in nucleation site density and accessibility. Direct observation under liquid conditions highlights the critical role of bacterial cell surface charges and exopolymer types in metal mineralization. This has strong environmental implications because biofilms structured by exopolymers are widespread in nature and constitute the main form of microbial life on Earth.

INTRODUCTION

Biomineralization driven by bacteria is a major environmental process that controls immobilization, transport, speciation, and even toxicity of metal(loid)s (*1*). Hence, it constitutes a critical mechanism that governs metal(loid)s cycling on Earth, from soils to several kilometers below the ground's surface (*2*). Mineral precipitation primarily depends on the supersaturation of chemical species in a defined volume. In the vicinity of bacteria, this supersaturation can be locally favored by negatively charged functional groups located on bacterial cell walls (*3*), which attract and concentrate metallic cations. Biofilms are three-dimensional (3D) biological structures composed of extracellular polymeric substances in which microbial cells are encased. They represent the main organization mode of microorganisms on Earth, accounting for about 80% of all bacteria in surface environments (*4*). In these widespread biological structures, exopolymers are also thought to control metal(loids) mineralization (*5*–*7*). However, the exact role of bacterial cell envelopes and of exopolymers as nucleation templates for mineral formation remains largely unexplored under environmentally relevant conditions.

Given the high spatial resolution required to observe mineral/organic interactions at the submicrometer scale (*8*), conventional electron microscopy remains the preferred method for studying biominerals formation. However, this approach is limited by constraining preparation steps, including sample dehydration and chemical fixation. Among the main artifacts inherent to dehydration, shrinking of the fragile 3D structure of biofilms generates misleading information regarding the spatial location of mineralization at the bacterial cell surfaces and the exopolymer/mineral spatial relationships. Liquid-cell transmission electron microscopy has the potential to overcome these limitations by providing direct and time-resolved observations in aqueous media at the submicrometric scale (*9*, *10*). While this in situ technique has been extensively used to visualize the formation of inorganic nanostructures (*11*–*13*), including minerals (*14*–*16*), it has also emerged as a reliable method for studying the structure of biological materials—e.g., individual cells (*17*), extracellular vesicles (*18*), bacteria (*19*), bacteriophages (*20*), and their interactions (*21*)—in liquid media. Nevertheless, the possibility of directly observing mineralization processes on microbial cells and their exopolymeric matrix under realistic conditions would constitute an undeniable advance opening new research avenues. It is well established, however, that during liquid-cell scanning transmission electron microscopy (LC-STEM) experiments, beam-induced radiolysis of water generates hydrated electrons and reactive oxygen species. These species reach a steady-state concentration within a second, depending on the electron dose rate (*22*). We have taken advantage of these radiolytic effects to study the mineralization of redox-sensitive Mn on bacterial cell wall and surrounding self-secreted exopolymers.

To better understand the role of the physical and chemical properties of bacterial surfaces (i.e., of cell walls and associated exopolymers) in providing sites for mineral nucleation and growth, we used, in Mn-bearing aqueous solutions, two strains of *Escherichia coli* that differ in the nature of the exopolymers they secrete. The strain *E. coli* 1094 2K7 (hereafter referred to as 2K7) produces abundant and dense cellulosic polymers constitutive of the biofilm matrix (*23*, *24*), while the strain *E. coli* K12 MG1655 MGF-Δ*traD* (hereafter referred to as MGF), carrying the F plasmid, is characterized by the production of a proteinaceous conjugative F pilus, allowing cell surface contact promoting biofilm formation (*25*). In its planktonic form, MGF does not produce bulky exopolymers around the bacterial cell but rather nascent pili on the bacteria surface. To compare the role of each exopolymer in nucleation and mineral growth, bacteria were loaded in a liquid cell with an aqueous solution containing Mn, in two duplicate independent experiments, and the effects of exposure to an electron beam were studied.

[1]Université de Paris, Institut de physique du globe de Paris, CNRS, 75238 Paris Cedex 05, France. [2]Université de Paris, Laboratoire Matériaux et Phénomènes Quantiques, CNRS, 75013 Paris, France. [3]Institut de Minéralogie, de Physique des Matériaux et de Cosmochimie, Sorbonne Université, IRD, Muséum National d'Histoire Naturelle, CNRS, Campus Pierre et Marie Curie, 75252 Paris Cedex 05, France. [4]Unité de Génétique des Biofilms, Institut Pasteur, 75015 Paris, France.
*Present address: GFZ German Research Center for Geosciences, Telegrafenberg, 14473 Potsdam, Germany.
†Corresponding author. Email: damien.alloyeau@univ-paris-diderot.fr (D.A.); gelabert@ipgp.fr (A.G.)

RESULTS AND DISCUSSION

In situ observations of mineralizing bacterial cells

First, we highlight the effect of Mn precursors on the contrast and stability of bacterial cells during LC-STEM imaging. Because of the low electron contrast of biological materials through 250 to 500 nm of liquid (see Materials and Methods), LC-STEM imaging usually requires contrasting agents such as uranyl acetate (26) or gold nanoparticles (18, 27). However, the study of metal mineralization processes is impossible in the presence of other metals that may interfere in mineral formation. When bacterial cells are imaged in an aqueous solution containing Mn^{2+} precursors, their signal-to-noise ratio increases with time under electron irradiation (Figs. 1 and 2). This results from the electron beam–induced formation of a Mn-bearing mineral shell on bacterial cell surfaces, as revealed by energy-dispersive X-ray spectrometry (EDXS) (Fig. 3). Moreover, although this continuous in situ monitoring exposes the bacteria to a high cumulative electron dose (d_{TOT}) of up to 845 e^- $Å^{-2}$ (Fig. 1A), no breaking of the bacterial cell wall or notable shrinkage of the inner volume of bacterial cells is observed. On the contrary, in the absence of $MnCl_2$ in the experimental solution, there is no mineralization on the cell surface and the bacterial cell wall is systematically disrupted as of a d_{TOT} of 100 e^- $Å^{-2}$, as highlighted in the control experiment shown in fig. S1. We postulate that Mn protects the cell wall from deleterious oxidoreductive damages, thus avoiding visible destruction of the bacterial structure and cell interior leakage during LC-STEM experiments. We acknowledge that this in situ LC-STEM imaging does not allow visualization of possible nano- to molecular-scale damage to cell membranes and their components. Controversial studies have examined the viability of living cells, including bacteria, during LC-STEM experiments (26, 28, 29), but it is very likely that these microorganisms are no longer in a physiologically active state when exposed to electron doses higher than 10^{-5} e^- $Å^{-2}$ (30). Nevertheless, regardless of their living state, the precipitation observed on the two bacterial strains investigated here provides new insights into the role as template of cell surface and exopolymer on Mn mineralization processes under hydrous conditions.

Homogeneous mineral formation on MGF cell surface

Mn accumulation on single MGF and 2K7 bacterial cells is illustrated in Figs. 1 and 2, respectively, with duplicate experiments presented in fig. S2. Under low–electron dose rate conditions (0.30 e^- $Å^{-2}$ s^{-1}), Mn precipitation on MGF cells results in the formation of a thin and smooth layer that homogeneously covers the cell surface (Fig. 1A). The thickness of this Mn-rich shell reaches 11 nm after 420 s of irradiation, with an electron dose rate of 0.30 e^- $Å^{-2}$ s^{-1}. Therefore, at this electron dose rate, the mineral growth rate is calculated at 1.6 nm min^{-1} (Materials and Methods). However, when the same bacterial cell is then exposed to a higher electron dose rate (5.23 e^- $Å^{-2}$ s^{-1}), we observe the formation of a 84-nm-thick shell with increasingly rougher surfaces in 110 s (Fig. 1B). Therefore, at an electron dose rate of 5.23 e^- $Å^{-2}$ s^{-1}, the mineral growth rate is 45.8 nm min^{-1}. The evolution of the mineralized cell surface area as a function of d_{TOT} (Fig. 1C) indicates the increase in Mn growth rate with the electron dose rate. This, in turn, indicates that radiolysis is the driving force of the precipitation reaction in the system investigated. Nevertheless, the key role of biological matrices as a nucleation template is demonstrated by the absence of Mn precipitate in the surrounding aqueous medium or in blank experiments (i.e., without bacterial cells) performed at similar electron dose rates (fig. S3).
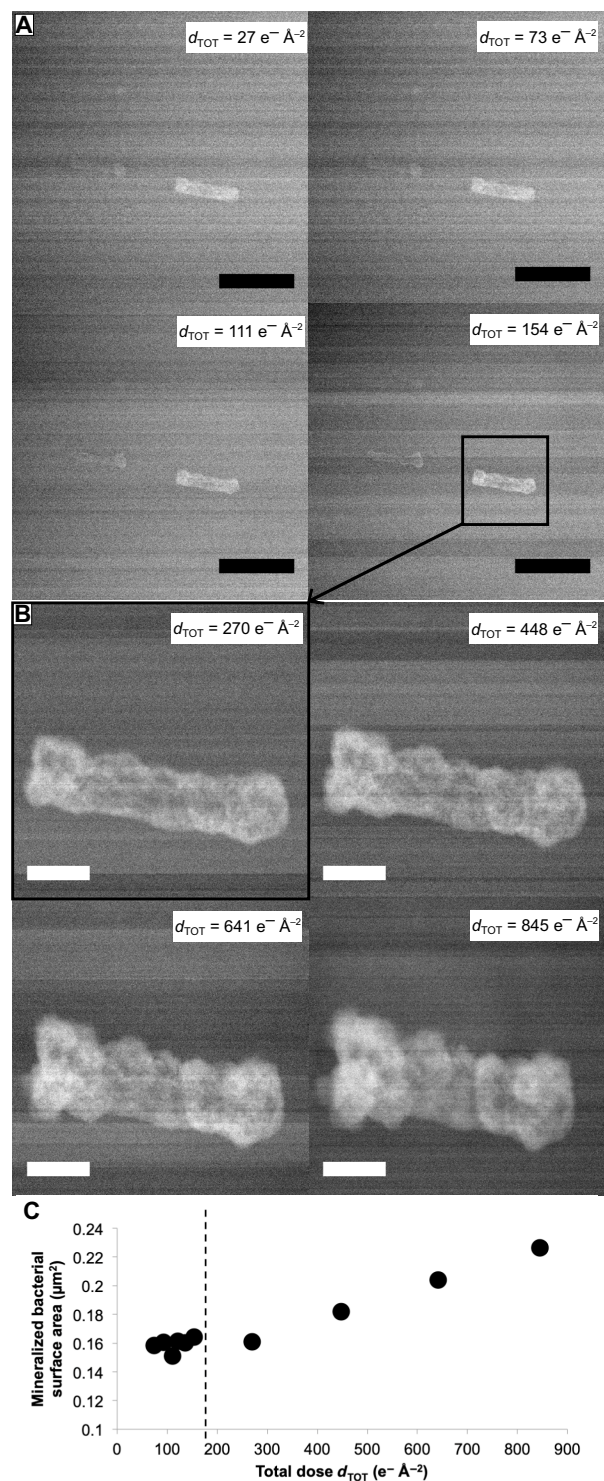

Fig. 1. In situ monitoring of Mn bacterial mineralization. (**A**) Time series of LC-STEM images acquired with a continuous electron dose rate of 0.30 e^- $Å^{-2}$ s^{-1} on a cell of *E. coli* MGF bathed in an aqueous solution containing Mn. Scale bars, 1 μm. (**B**) Time series of LC-STEM images of the same cell subsequently irradiated with a continuous electron dose rate of 5.23 e^- $Å^{-2}$ s^{-1} at increased magnification. Scale bars, 200 nm. d_{TOT} is the cumulative electron dose in e^- $Å^{-2}$ calculated for each image. (**C**) Mineralized bacterial cell surface area as a function of cumulative electron dose. Dashed line indicates the change in magnification (i.e., increase in the dose rate).
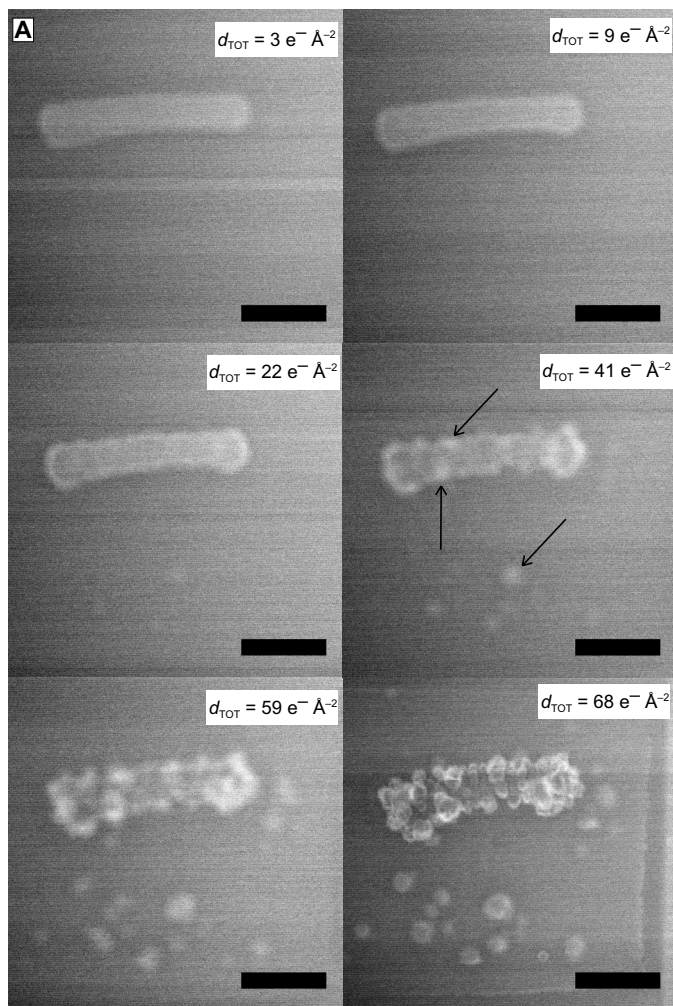
Fig. 2. Exopolymers secreted by bacteria influence Mn mineralization. (A) Time series of LC-STEM images acquired with a continuous electron dose rate of 0.30 e$^-$ Å^{-2} s^{-1} on a cell of *E. coli* 2K7 bathed in an aqueous solution containing Mn. Scale bars, 1 μm. Black arrows show mineral particles that nucleate on the bacterial cell wall and in the Mn-bearing solution. d_{TOT} is the cumulative electron dose in e$^-$ Å^{-2} calculated for each image. **(B)** Size of mineral particles grown on (white circles) or near (black triangles) the bacterial cell wall as a function of the cumulative electron dose.

Fig. 3. STEM-EDXS characterization of the mineral crusts formed on the bacterial cell wall. Solid line spectrum is the signal obtained with the electron probe on the mineralized bacteria *E. coli* MGF, and dashed spectrum corresponds to the signal obtained in the surrounding aqueous solution. The strong oxygen signal in the latter likely relates to water.

Heterogeneous mineral formation on 2K7 cell surface and its surrounding

The dense cellulosic matrix secreted by strain 2K7 provides a different reactive environment for Mn mineralization. As a result, two notable di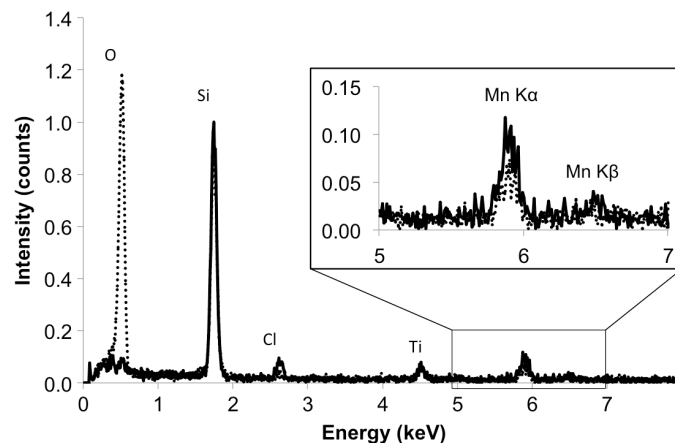fferences in mineral formation characteristics are observed between MGF and 2K7 strains. The first difference observed between the two strains is that under an electron dose rate of 0.30 e$^-$ Å^{-2} s^{-1}, nucleation and growth of individual Mn-containing nanoparticles on the surface of 2K7 cells are observed (Fig. 2A). The size of these isolated nanoparticles increases linearly with d_{TOT} (Fig. 2B), with diameters ranging between 200 and 300 nm at d_{TOT} of 68 e$^-$ Å^{-2}. Thus, under similar low–electron dose conditions (0.30 e$^-$ Å^{-2} s^{-1}), while a continuous shell forms on MGF cells (Fig. 1A and fig. S2A), a heterogeneous distribution of quasi-spherical Mn nanoparticles appears on 2K7 cells (Fig. 2A and fig. S2B). The two final mineralization morphologies are quantitatively differentiated by measuring the evolution in cell convexity (Fig. 4A and Materials and Methods). For both strains, convexity decreases with d_{TOT} and Mn particle/shell growth, hence reflecting an increase in surface roughness (Fig. 4B). For 2K7 strain, the steep drop in convexity at increasing d_{TOT} reflects the formation of individual 3D islands of Mn, while the overall homogeneous Mn shell formed around MGF cells shows a weaker decrease in convexity. The second difference observed between the two strains is the growth of Mn nanoparticles in the aqueous medium, in vicinity of 2K7 cells (Fig. 2). As such a mineralization is not observed in solution around MGF cells (Fig. 1), we infer that extracellular material is present in solution around 2K7 cells. It is worth noting that the presence of cellulose exopolymers near the surface of 2K7 cells was observed by Le Quéré and Ghigo (*31*). The size evolution of Mn particles growing on *E. coli* 2K7 exopolymers is identical to that of the particles growing on associated bacterial cell walls (Fig. 2B), suggesting similar growth processes. Under similar irradiation conditions, no precipitation occurs in the solution at a distance from the cells (fig. S3), indicating that the extracellular material is mainly located around 2K7 bacterial cells.

Surface charge as a control of the dynamics of mineral formation

These two distinct Mn mineralization mechanisms revealed by LC-STEM (summarized in Fig. 4C), namely, the formation of individual nanoparticles versus homogeneous precipitation around bacterial
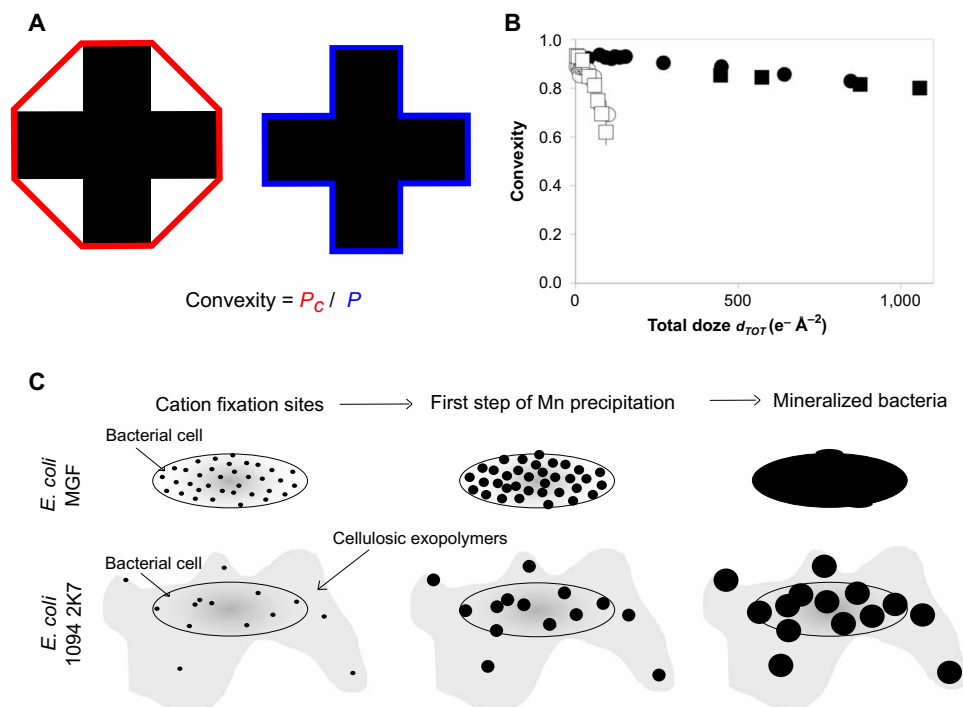
Fig. 4. Contrasted nucleation and growth mechanisms of Mn precipitates as a function of bacterial exopolymers. (**A**) Schematic representation of convexity. It corresponds to the ratio between effective perimeter (*P*, in blue) and convex perimeter (*P*$_C$, in red) of a 2D shape. (**B**) Convexity of mineralized bacterial cells and their exopolymers as a function of the cumulative electron dose. Black squares and circles were obtained from two duplicate measurements on individual *E. coli* MGF cells (Fig. 1 and fig. S2A). White squares and circles were obtained from two duplicate measurements on individual *E. coli* 2K7 cells (Fig. 2 and fig. S2B). (**C**) Schematic representation of mineral formation for both strains. Black circles depict Mn precipitates.

cells, depend on chemical site density on the cell surface and within the exopolymers produced by these bacterial strains. Bacterial surfaces are negatively charged at neutral pH due to the presence of deprotonated carboxylic groups (pK_a, where K_a is the acid dissociation constant, in the range of 4.6 to 5.4) and partially deprotonated phosphoryl groups (pK_a in the range of 6.6 to 7.8) (*32*). Such negatively charged functional sites promote cation adsorption and subsequent mineral precipitation (*3, 5*). Electrophoretic mobility, which is directly related to the overall charge on the bacterial cell surface, was determined by measuring bacterial cell migration velocity in an applied electric field of known intensity. This electrophoretic mobility is 10 times more negative for MGF strain over the entire pH range investigated (between pH 4 and 11), as compared to 2K7 strain (Fig. 5). This reflects a substantially higher density of negatively charged sites on MGF cell surfaces, compared to 2K7 cell surfaces and their associated cellulosic exopolymers. With regard to the mineralization processes, a high density of negatively charged functional groups provides numerous sites for cation adsorption, which results in a high number of nucleation sites and favors homogeneous mineralization on MGF cell surfaces (Fig. 4C). On the contrary, cellulose produced around 2K7 cells only exhibits poorly polarized hydroxyl functions, while the bulky structure of this biopolymeric layer would reduce access to the functionalized bacterial surfaces. Therefore, 2K7 cells have a limited number of negatively charged reactive sites that promote nucleation, resulting in the growth of isolated Mn-mineral islands. In addition, the formation of Mn particles with similar growth dynamics in the vicinity of 2K7 bacterial
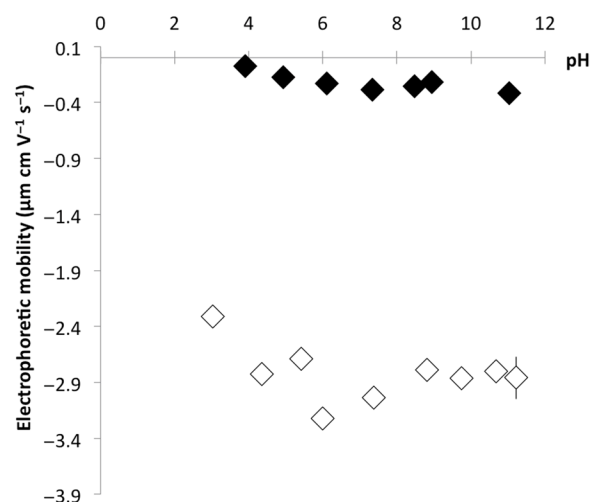

Fig. 5. Electrophoretic mobility as a function of pH. Black and white diamonds refer to *E. coli* 2K7 and *E. coli* MGF, respectively.

cells indicates the presence of nucleation sites in the surrounding cellulose matrix (Figs. 2A and 4C and fig. S2B).

From a technical perspective, the present study demonstrates the possibility of using radiolysis induced by the incident electron beam to trigger and monitor mineralization processes involving redox-sensitive elements during LC-STEM experiments. Noticeably, all these

observations were conducted in the absence of additional contrasting agents. These in situ observations at the submicrometric scale confirm the predominant role of the physical and chemical properties of bacterial cell surfaces during mineralization, as already reported for specific proteins (*33*). The growth process and final morphology of Mn-bearing precipitates formed on bacterial cells depend on the density of cation fixation sites, which is dictated by their surface charge and by the nature and spatial distribution of the associated exopolymers. These findings emphasize the fundamental role of exopolymers in biomineralization process and, consequently, in metal sequestration in the environment. Given the ubiquity of microbial biofilms in nature (*4*), and the recent evidence that microorganisms produce extracellular reactive oxygen species (*34*) capable of modifying the cycling of redox-active elements, these results find direct applications in assessing metal mobility and bioavailability in natural systems. However, given the large variability in the nature of exopolymers and in microbial surface properties, further investigations are required to better constrain the role of biofilm-forming microorganisms during mineralization and, consequently, their impact on metal cycling in the environment.

MATERIALS AND METHODS

Experimental design
Two different strains of *E. coli* forming different types of exopolymers were suspended in a Mn-bearing aqueous solution and loaded into a liquid cell in two independent and duplicate experiments. They were then observed under electron beam irradiation using LC-STEM.

Bacterial strains
This study was conducted using bacterial mutants of *E. coli* strains generated at Institut Pasteur (France). The first mutant was *E. coli* K12 MG1655 MGF-Δ*traD* plasmid (referred to as MGF in this study) carrying a transfer-deficient F conjugative plasmid. The latter is responsible for the production of proteinaceous F pili that promote cell surface contact and hence biofilm formation (*25*). In terms of chemical functions carried, pili are made up of specific proteins called pilins. These proteins contain carboxylic and amine functions and some adsorbed residual phosphates. The second mutant was *E. coli* 1094 2K7 (referred to as 2K7 in this study). This strain is characterized by an enhanced production of cellulose around the bacterial cell (*23*, *24*), with cellulose molecules exhibiting only poorly polarized hydroxyl functions.

Sample preparation
Bacteria were first grown overnight under agitation at 25°C in sterile Falcon tubes filled with 30 ml of lysogeny broth (LB)–rich medium. Cells were then washed three times with a sterile aqueous solution containing 10 mM NaCl and 5 mM Na-acetate. Then, 1 ml of the bacterial suspension at an optical density at 600 nm of 1 was exposed to 50 mM $MnCl_2$ in an aqueous solution composed of 2 mM $(NH_4)_2SO_4$, 0.7 mM NaCl, 10 mM Hepes, and 1 mM D-glucose and directly observed by transmission electron microscopy. All the chemical reagents from Sigma-Aldrich were of high-purity grade.

Liquid-cell scanning transmission electron microscopy
LC-STEM experiments were performed on a JEOL ARM 200F microscope equipped with a Correction Electron Optical System (CEOS) aberration corrector for the objective lens and a cold field-emission gun electron source. The experiments were carried out with an acceleration voltage of 200 kV.

The liquid cells are commercialized by Protochips Inc. (Morrisville, USA). They consist of two silicon wafers with dimensions of 2 mm by 2 mm and 4.5 mm by 6 mm, referred to as the small and large E-chips, respectively. Each E-chip has a 550 μm–by–50 μm window covered with a 50-nm-thick amorphous silicon nitride (SiN) film. A 2-μl drop of the sample containing the bacterial cells has been deposited on the electron-transparent SiN membrane of the small E-chip. The large E-chip was then placed over the small one with their windows in cross-configuration, giving a square field of view with an edge length of 50 μm. Therefore, the drop of solution was squeezed between the two E-chips in a volume defined by the thickness of the gold spacers of the small E-chip (150 nm in our case). The lid of the holder tip resulting in a vacuum-sealed liquid cell then closed the entire chamber.

LC-STEM experiments were performed in STEM mode by using a high-angle annular dark-field detector (STEM-HAADF), without changing the condenser aperture (20 μm) and the spot size (5C, below 1 nm in size) to maintain a constant beam current of 9.07×10^6 e$^-$ s^{-1}. All the STEM-HAADF images were acquired with a size of 1024 by 1024 pixels, a pixel dwell time of 10 μs, and an angular range of detection of 54 to 200 mrad. Between the acquisitions of these images, Mn mineralization was observed continuously under high-speed imaging conditions (image size of 512 by 512 pixels and dwell time of 5 μs). The electron dose rate was calculated by dividing the beam current by the surface area irradiated by the beam (i.e., the size of the images in STEM mode). The cumulative electron dose (or total electron dose, d_{TOT}) indicated in each image shown in Figs. 1 and 2 and figs. S1 to S3 was calculated by multiplying the dose rate by the irradiation time, taking into account any possible changes in magnification during observations. The contrast of the observation window was regularly checked in low-magnification mode to ensure that the liquid cell was always fully filled with the experimental aqueous solution during the experiment. STEM-HAADF imaging was preferentially performed in the corner of the observation window where the smallest liquid thicknesses are found (between 250 and 500 nm with 150-nm gold spacers) (*18*). Because of the outward bowing of the SiN membranes under vacuum, the liquid thickness was not homogeneous in the liquid cell.

We have selected 10 images collected during the experiment performed using MGF cells (8 of them are shown in Fig. 1, A and B) to measure the surface area of the mineralized bacterial cells and the precipitate thickness using Digital Micrograph (Gatan). For 2K7 cells, we focused on 11 representative growing particles. Five of these particles were on the bacterial cell wall, and six were among those that formed next to the bacterial cell. Their size was measured on five STEM images of increasing d_{TOT} (only three of them are shown in Fig. 2A: 41, 59, and 68 e$^-$ Å^{-2}) using ImageJ software (*35*).

Mineral growth measurements
To estimate mineral growth on the surface of *E. coli* MGF cells, we approximated that the 2D projection of the bacterial cell in the LC-STEM images is an ellipse. Therefore, before irradiation, the measured surface area of the bacteria corresponds to $ab\pi$, with a and b being the major and minor radii, respectively. The electron beam irradiation has resulted in a homogeneous mineralization on the bacterial cell surface. Hence, after electron beam exposure, the inferred mineralized bacterial surface area γ becomes $(a + x)(b + x)\pi$, where x is the mineral thickness. As the surface areas before and

after electron beam irradiations were measured on the LC-STEM images, it was possible to solve the resulting quadratic equation $\pi x^2 + ab\pi^2 x + ab\pi = 0$ to estimate the mineral thickness formed during electron beam irradiation.

Convexity measurements

Three repeated contours of mineralized bacterial cells and particles were hand-performed on each image to estimate their surface areas while reducing possible bias in the measurements. Convexity values of the mineralized bacterial cells and of the particles carried by the exopolymers were then obtained using Digital Micrograph software.

Electrophoretic mobility

Electrophoretic mobility measurements were performed on Zetasizer Nano ZS (Malvern Panalytical). For these experiments, bacteria were first grown overnight in LB-rich medium and then washed three times with a sterile aqueous solution made of 10 mM NaCl and 5 mM Na-acetate. They were further suspended in an aqueous solution containing 2 mM $(NH_4)_2SO_4$, 0.7 mM NaCl, and 10 mM Hepes for electrophoretic mobility analysis. Samples consisted of a 25-ml bacterial suspension with known pH. The pH was adjusted to values between 4 and 11 using NaOH and HNO_3 solutions.

Statistical significance

Duplicate mineralization experiments were performed by exposing intact bacterial cells from each strain to the electron beam (Figs. 1 and 2 and fig. S2). During data processing, each cell, particle size, and shape measurements were performed independently three times to assess measurement error.

SUPPLEMENTARY MATERIALS

Supplementary material for this article is available at http://advances.sciencemag.org/cgi/content/full/6/27/eaaz3125/DC1

View/request a protocol for this paper from *Bio-protocol*.

REFERENCES AND NOTES

1. G. M. Gadd, Geomicrobiology of the built environment. *Nat. Microbiol.* **2**, 16275 (2017).
2. B. Ménez, V. Pasini, F. Guyot, K. Benzerara, S. Bernard, D. Brunelli, Mineralizations and transition metal mobility driven by organic carbon during low-temperature serpentinization. *Lithos* **323**, 262–276 (2018).
3. T. J. Beveridge, R. G. Murray, Uptake and retention of metals by cell walls of *Bacillus subtilis*. *J. Bacteriol.* **127**, 1502–1518 (1976).
4. H.-C. Flemming, S. Wuertz, Bacteria and archaea on Earth and their abundance in biofilms. *Nat. Rev. Microbiol.* **17**, 247–260 (2019).
5. S. Schultze-Lam, D. Fortin, B. S. Davis, T. J. Beveridge, Mineralization of bacterial surfaces. *Chem. Geol.* **132**, 171–181 (1996).
6. C. Dupraz, P. T. Visscher, L. K. Baumgartner, R. P. Reid, Microbe-mineral interactions: Early carbonate precipitation in a hypersaline lake (Eleuthera Island, Bahamas). *Sedimentology* **51**, 745–765 (2004).
7. C. S. Chan, S. C. Fakra, D. C. Edwards, D. Emerson, J. F. Banfield, Iron oxyhydroxide mineralization on microbial extracellular polysaccharides. *Geochim. Cosmochim. Acta* **73**, 3807–3818 (2009).
8. S. Behrens, A. Kappler, M. Obst, Linking environmental processes to the *in situ* functioning of microorganisms by high-resolution secondary ion mass spectrometry (NanoSIMS) and scanning transmission X-ray microscopy (STXM). *Environ. Microbiol.* **14**, 2851–2869 (2012).
9. N. de Jonge, F. M. Ross, Electron microscopy of specimens in liquid. *Nat. Nanotechnol.* **6**, 695–704 (2011).
10. F. M. Ross, Opportunities and challenges in liquid cell electron microscopy. *Science* **350**, 6267 (2015).
11. D. Alloyeau, W. Dachraoui, Y. Javed, H. Belkahla, G. Wang, H. Lecoq, S. Ammar, O. Ersen, A. Wisnet, F. Gazeau, C. Ricolleau, Unravelling kinetic and thermodynamic effects on the growth of gold nanoplates by liquid transmission electron microscopy. *Nano Lett.* **15**, 2574–2581 (2015).
12. N. Ahmad, Y. Le Bouar, C. Ricolleau, D. Alloyeau, Growth of dendritic nanostructures by liquid-cell transmission electron microscopy: A reflection of the electron-irradiation history. *Adv. Struct. Chem. Imaging* **2**, 9 (2016).
13. H.-G. Liao, K. Niu, H. Zheng, Observation of growth of metal nanoparticles. *Chem. Commun.* **49**, 11720–11727 (2013).
14. P. J. M. Smeets, K. R. Cho, R. G. E. Kempen, N. A. J. M. Sommerdijk, J. J. De Yoreo, Calcium carbonate nucleation driven by ion binding in a biomimetic matrix revealed by in situ electron microscopy. *Nat. Mater.* **14**, 394–399 (2015).
15. X. Wang, J. Yang, C. M. Andrei, L. Soleymani, K. Grandfield, Biomineralization of calcium phosphate revealed by in situ liquid-phase electron microscopy. *Commun. Chem.* **1**, 80 (2018).
16. M. H. Nielsen, S. Aloni, J. J. D. Yoreo, In situ TEM imaging of $CaCO_3$ nucleation reveals coexistence of direct and indirect pathways. *Science* **645**, 1158 (2014).
17. M. J. Dukes, D. B. Peckys, N. de Jonge, Correlative fluorescence microscopy and scanning transmission electron microscopy of quantum-dot-labeled proteins in whole cells in liquid. *ACS Nano* **4**, 4110–4116 (2010).
18. M. Piffoux, N. Ahmad, J. Nelayah, C. Wilhelm, A. Silva, F. Gazeau, D. Alloyeau, Monitoring the dynamics of cell-derived extracellular vesicles at the nanoscale by liquid-cell transmission electron microscopy. *Nanoscale* **10**, 1234–1244 (2018).
19. T. J. Woehl, S. Kashyap, E. Firlar, T. Perez-Gonzalez, D. Faivre, D. Trubitsyn, D. A. Bazylinski, T. Prozorov, Correlative electron and fluorescence microscopy of magnetotactic bacteria in liquid: Toward in vivo imaging. *Sci. Rep.* **4**, 6854 (2015).
20. A. Cameron Varano, A. Rahimi, M. J. Dukes, S. Poelzing, S. M. McDonald, D. F. Kelly, Visualizing virus particle mobility in liquid at the nanoscale. *Chem. Commun.* **51**, 16176–16179 (2015).
21. W. J. Dearnaley, B. Schleupner, A. C. Varano, N. A. Alden, F. Gonzalez, M. A. Casasanta, B. E. Scharf, M. J. Dukes, D. F. Kelly, Liquid-cell electron tomography of biological systems. *Nano Lett.* **19**, 6734–6741 (2019).
22. N. M. Schneider, M. M. Norton, B. J. Mendel, J. M. Grogan, F. M. Ross, H. H. Bau, Electron–water interactions and implications for liquid cell electron microscopy. *J. Phys. Chem. C* **118**, 22373–22382 (2014).
23. S. Da Re, J.-M. Ghigo, A CsgD-independent pathway for cellulose production and biofilm formation in *Escherichia coli*. *J. Bacteriol.* **188**, 3073–3087 (2006).
24. J. Bernal-Bayard, L. Gomez-Valero, A. Wessel, V. Khanna, C. Bouchier, J.-M. Ghigo, Short genome report of cellulose-producing commensal *Escherichia coli* 1094. *Stand Genomic Sci.* **13**, 13 (2018).
25. J.-M. Ghigo, Natural conjugative plasmids induce bacterial biofilm development. *Nature* **412**, 442–445 (2001).
26. E. Kennedy, E. M. Nelson, T. Tanaka, J. Damiano, G. Timp, Live bacterial physiology visualized with 5 nm resolution using scanning transmission electron microscopy. *ACS Nano* **10**, 2669–2677 (2016).
27. N. De Jonge, D. B. Peckys, G. J. Kremers, D. W. Piston, Electron microscopy of whole cells in liquid with nanometer resolution. *Proc. Natl. Acad. Sci. U.S.A.* **106**, 2159–2164 (2009).
28. N. de Jonge, D. B. Peckys, Live cell electron microscopy is probably impossible. *ACS Nano* **10**, 9061–9063 (2016).
29. E. Kennedy, E. M. Nelson, J. Damiano, G. Timp, Gene expression in electron-beam-irradiated bacteria in reply to "Live cell electron microscopy is probably impossible". *ACS Nano* **11**, 3–7 (2017).
30. L. Reimer, H. Kohl, *Transmission Electron Microscopy: Physics of Image Formation* (Springer-Verlag, ed. 5, 2008).
31. B. Le Quéré, J.-M. Ghigo, BcsQ is an essential component of the *Escherichia coli* cellulose biosynthesis apparatus that localizes at the bacterial cell pole. *Mol. Microbiol.* **72**, 724–740 (2009).
32. N. Yee, J. B. Fein, Quantifying metal adsorption onto bacteria mixtures: A test and application of the surface complexation model. *Geomicrobiol. J.* **20**, 43–60 (2003).
33. S. Kashyap, T. Woehl, C. Valverde-Tercedor, M. Sánchez-Quesada, C. Jiménez López, T. Prozorov, Visualization of iron-binding micelles in acidic recombinant biomineralization protein, MamC. *J. Nanomater.* **2014**, 1–7 (2014).
34. J. M. Diaz, C. M. Hansel, B. M. Voelker, C. M. Mendes, P. F. Andeer, T. Zhang, Widespread production of extracellular superoxide by heterotrophic bacteria. *Science* **340**, 1223–1226 (2013).
35. C. A. Schneider, W. S. Rasband, K. W. Eliceiri, NIH Image to ImageJ: 25 years of image analysis. *Nat. Methods* **9**, 671–675 (2012).

Citation: T. Couasnon, D. Alloyeau, B. Ménez, F. Guyot, J.-M. Ghigo, A. Gélabert, In situ monitoring of exopolymer-dependent Mn mineralization on bacterial surfaces. *Sci. Adv.* **6**, eaaz3125 (2020).